https://doi.org/10.5194/egusphere-2026-3175
Preprint. Discussion started: 3 July 2026

An Emergent Warming-Linked Mode of Cloud Cover in Reanalyses: Systematically Missing in CMIP6 AMIP Simulations

Shutian Mu[1], Huan Liu[1], Jiazhen Zhao[1], Xiaoqiao Wang[1], Fangying Wu[1], Lei Liu[1]

[1]College of Meteorology and Oceanography, National University of Defense Technology, Changsha, 410073, China.

Correspondence to: Huan Liu (huanliu@nudt.edu.cn)

Abstract. Cloud feedback remains the dominant source of uncertainty in climate projections, highlighting the necessity of rigorous cloud-based evaluations of climate models. Current assessments rely predominantly on cloud climatology and responses to internal variability, leaving cloud changes driven by historical warming largely unassessed. Here, we identify an emergent trend mode in total cloud cover (CLT) across multiple reanalysis products that is closely linked to global mean surface temperature. Using this warming-linked mode as the primary benchmark, we evaluate 13 CMIP6 AMIP simulations (1979–2014). While the models adequately capture global warming and internal variability in both temperature and CLT, this CLT trend mode is systematically absent in the simulations. Diagnostic regression reveals that this absence is characterized by a substantial underestimation of the response amplitude and large-scale spatial mismatches. This systematic deficiency points to shared structural limitations in current atmospheric models. Addressing this specific discrepancy offers a targeted pathway to constrain the forced cloud response, thereby reducing cloud feedback uncertainties in future climate projections.

1 Introduction

Global mean surface temperature (GMST) has risen by approximately 1.1°C since the pre-industrial era (Gulev et al., 2021). This warming alters cloud properties, and the resulting cloud feedback constitutes the single largest source of uncertainty in climate projections (Stephens, 2005; Forster et al., 2021). While the Intergovernmental Panel on Climate Change (IPCC) Sixth Assessment Report (AR6) concludes with high confidence that the net cloud feedback is positive (i.e., amplifying warming), its magnitude remains poorly constrained (Cess et al., 1990; Zelinka et al., 2017; Forster et al., 2021; Zhang et al., 2022). This persistent uncertainty stems largely from the inadequate representation of cloud processes in climate models (Forster et al., 2021), necessitating rigorous cloud-based evaluations. Among various cloud properties, total cloud cover (CLT) is a primary determinant of cloud radiative effects (Qian et al., 2012; Zhao et al., 2022) and serves as a fundamental metric for such evaluations. Consequently, assessing the fidelity of model-simulated CLT, particularly its response to historical warming, is critical for constraining cloud feedback estimates.

Direct evaluations of historical CLT trends face inherent observational limitations, as satellite records are often too short or subject to temporal inhomogeneities to robustly isolate the forced signal (Chepfer et al., 2014; Aerenson et al., 2022). Furthermore, conventional local trend analyses tend to obscure the large-scale, spatially coherent signatures associated with warming-driven cloud changes (Norris & Evan, 2015; Norris et al., 2016). As a result, current CLT-based performance evaluations predominantly rely on two types of benchmarks: climatological means (Probst et al., 2012; Wang & Su, 2013; Enriquez-Alonso et al., 2016; Ceppi et al., 2024) and modes of internal variability, such as the El Niño-Southern Oscillation (ENSO) (Wang & Su, 2015; Wang et al., 2024). To date, these approaches have been effective in characterizing quasi-equilibrium states and diagnosing systematic model biases. For instance, ENSO-based spatial decompositions have revealed systematic biases in tropical cloud changes and longwave feedbacks (Wang & Su, 2015; Wang et al., 2024). However, skill in simulating climatological means and internal variability does not guarantee a reliable simulation of the forced response. Consequently, a model may satisfy traditional evaluations even when its forced warming signal is absent, as the weak trend is statistically masked by dominant internal variability. This underscores a critical gap in the direct evaluation of the forced cloud response to historical warming.

To partly bridge this gap, we shift the evaluation focus to a warming-linked CLT mode. Building on the mode initially identified in the European Centre for Medium-Range Weather Forecasts 5th Generation Reanalysis (ERA5) (Liu et al., 2023), we confirm its presence across multiple reanalysis products and establish it as the best available estimate of the large-scale forced cloud response. Using this as a primary diagnostic benchmark, we evaluate CLT simulations from 13 climate models, revealing a systematic absence of this emergent trend mode across all of them. Diagnostic regression indicates that this absence is characterized by substantial underestimation of the response amplitude and large-scale spatial mismatches.

2 Data and Methods

2.1 Data

This study uses simulations from the Atmospheric Model Intercomparison Project (AMIP), atmospheric reanalyses, satellite observations, and the Niño 3.4 index, primarily focusing on monthly near-surface air temperature (TAS) and CLT. The analysis employs two distinct periods tailored to specific objectives: 1979–2014, the standard period for AMIP experiments, for mode extraction and model evaluation; and 2003–2021 to constrain reanalysis uncertainties against independent satellite observations.

(1) AMIP simulations (1979–2014). We analyze AMIP simulations from 13 climate models (Table 1), which include both conventional/traditional global climate models (GCMs) and Earth system models (ESMs). All 13 models participated in the Cloud Feedback Model Intercomparison Project Phase 3 (CFMIP3; Webb et al., 2017) conducted under the Coupled Model Intercomparison Project Phase 6 (CMIP6; Eyring et al., 2016; Zhou et al., 2019). By prescribing observed sea surface temperatures and sea ice concentrations, AMIP experiments isolate the atmospheric response, filtering out the confounding effects of sea surface temperature biases inherent in coupled models (Eyring et al., 2016). This experimental design thus provides a robust baseline for evaluating atmospheric model performance (Ringer et al., 2014; Webb et al., 2017).

(2) Atmospheric reanalyses. This study uses four reanalyses that collectively cover the period 1979–2021 (though individual products have slightly different start years). Among them, ERA5 (Hersbach et al., 2023) over 1979–2014 serves as the primary

https://doi.org/10.5194/egusphere-2026-3175
Preprint. Discussion started: 3 July 2026

baseline for identifying the warming-linked CLT mode. Within ERA5' assimilation framework, TAS and CLT are derived through distinct processes: TAS is constrained by directly assimilated observations, whereas CLT is a diagnostic variable governed by the host model's cloud parameterizations (Barker, 2008; Hersbach et al.,2020). To account for these structural uncertainties in reanalysis-derived CLT, we incorporate three additional reanalyses: the Modern-Era Retrospective analysis for Research and Applications version 2 (MERRA-2; start from 1980; GMAO, 2015), the CMA Global Atmospheric Reanalysis Version 1.5 (CRA1.5; Zhang et al., 2025), and NCEP-DOE AMIP-II Reanalysis (R-2; Kanamitsu et al., 2002). Because these products employ distinct data assimilation systems and cloud parameterization schemes, they are ideal for two purposes. First, they cross-validate the robustness of the ERA5-derived trend mode during 1979–2014 (the one-year mismatch for MERRA-2 is negligible for this validation). Second, they help determine which dataset most reliably represents satellite observed CLT variability during the 2003–2021 period.

(3) Satellite observations (2003–2021). To provide an independent reference for evaluating the reanalysis products, we use daily CLT data from the Moderate Resolution Imaging Spectroradiometer (MODIS; Platnick et al., 2015) aboard the Aqua satellite as the observational benchmark for assessing reanalysis-derived CLT variability over the common period.

(4) Niño 3.4 index (1979–2014). To compare model performance in simulating the warming signal relative to internal variability, we use the "Clim-Adjusted" monthly Niño 3.4 index from the National Oceanic and Atmospheric Administration (NOAA) Climate Prediction Center. This index employs a dynamically centered 30-year base period to remove multi-decadal warming trends, thereby isolating the interannual ENSO signal.

Table 1: Information of the 13 AMIP simulations.

Model	Type	Center	Country	Reference	Variant	Horizontal Grids
IPSL-CM6A-LR	GCM	IPSL	France	Boucher et al. (2018)	r1i1p1f1	144 x 143
NorESM2-LM	ESM	NCC	Norway	Seland et al. (2019)	r1i1p1f1	144 x 96
HadGEM3-GC31-LL	GCM	MOHC	UK	Ridley et al. (2019)	r1i1p1f3	192 x 144
E3SM-1-0	ESM	UCSB, E3SM-Project, UCI	USA	Bader et al. (2019)	r1i1p1f1	360 x 180
MRI-ESM2-0	ESM	MRI	Japan	Yukimoto et al. (2019)	r1i1p1f1	320 x 160
GFDL-CM4	GCM	NOAA-GFDL	USA	Guo et al. (2018)	r1i1p1f1	360 x 180
CanESM5	ESM	CCCma	Canada	Swart et al. (2019)	r1i1p1f1	128 x 64
BCC-CSM2-MR	GCM	BCC	China	Wu et al. (2019)	r1i1p1f1	320 x 160
CESM2	ESM	NCAR	USA	Danabasoglu (2019)	r1i1p1f1	288 x 192
CNRM-CM6-1	GCM	CNRM-CERFACS	France	Voldoire (2018)	r1i1p1f2	256 x 128
GISS-E2-2-G	ESM	NASA-GISS	USA	NASA/GISS (2019)	r1i1p3f1	144 x 90
TaiESM1	ESM	AS-RCEC	China	Lee & Liang (2019)	r1i1p1f1	288 x 192
MIROC6	GCM	MIROC	Japan	Tatebe & Watanabe (2018)	r1i1p1f1	256 x 128

2.2 Data Processing

All analyses are conducted on annual means and annual anomalies at a uniform 1°×1° spatial resolution. Temporally, annual means are derived from monthly data (with daily MODIS data first aggregated into monthly means). Annual anomalies are then computed by removing the respective climatological means over their corresponding analysis periods (Section 2.1). Spatially, to ensure consistent spatial representation across datasets, all original monthly fields are bilinearly interpolated to the common 1°×1° grid prior to the calculation of annual means. To correct for the area distortion inherent in regular latitude-longitude grids, we apply area weighting (proportional to the cosine of the latitude) to all subsequent spatial statistics, including Empirical Orthogonal Function (EOF) analysis, spatial Pearson correlations, and spatial standard deviations.

2.3 Similarity Metrics

To quantify the cross-dataset consistency, we first extract their features using two methods: EOF decomposition (Hannachi et al., 2007) and linear regression (Wilks, 2011). Specifically, EOF decomposition provides the explained variance, spatial patterns (as EOFs), and temporal variations (as Principal Components, PCs) of corresponding variability modes. Linear regression, performed by regressing model anomalies onto the ERA5' PC, yields the explained variance and alternative spatial patterns (as slope maps) for the corresponding mode. Building on Coburn and Pryor (2021), we then develop five similarity metrics (Table 2) to evaluate the derived features across three physically meaningful aspects: one for variance, two for spatial patterns, and two for temporal variations of the modes. All metrics are normalized to the interval [-1, 1], except for S_{PSD}, which lies in [0, 1]. For all metrics, absolute values closer to 1 indicate higher similarity or stronger correlation. The definitions of these metrics are as follows (Eqs. 1–5):

Table 2: Information of the 5 similarity metrics.

Type	Metric name	Focus	Range
Explained variance metric	S_{VAR}	explained variance	(-1,1)
Spatial metrics	S_{SCORR}	spatial distribution	(-1,1)
	S_{SIGMA}	spatial dispersion	(-1,1)
Temporal metrics	S_{TCORR}	temporal phase	(-1,1)
	S_{PSD}	spectral characteristics	(0,1)

(1) S_{VAR}: The explained variance similarity metric

$$S_{VAR} = \begin{cases} 1 - \left|\frac{V_M - V_E}{V_E}\right|, 0 \le V_M \le V_E \\ -\left(1 - \left|\frac{V_M - V_E}{V_E}\right|\right), V_E < V_M \le 2V_E \\ 0, V_M > 2V_E \end{cases}, \tag{1}$$

where V_M and V_E represent the explained variances derived from datasets under evaluation (M) and the benchmark (E), respectively. The sign $(+/-)$ of S_{VAR} indicates their relative magnitude: a positive value means M has a lower explained variance than E, and a negative value means the opposite. For example, $\mathrm{S}_{\mathrm{VAR}} = 0.4$ implies V_M is 40% of V_E (a 60% deficit relative to V_E), while $\mathrm{S}_{\mathrm{VAR}} = -0.4$ implies V_M is 160% of V_E (a 60% excess relative to V_E).

(2) S_{SCORR}: The spatial distribution similarity metric

$$S_{SCORR} = r, \tag{2}$$

where r represents the weighted Pearson correlation coefficient between the spatial patterns of M and E. Values of 1 and -1 indicate perfect positive and negative linear association (i.e., identical and opposite spatial patterns), respectively. Values within about ±0.4 generally indicate no or only weak correlation.

(3) S_{SIGMA}: The spatial dispersion similarity metric

$$S_{SIGMA} = \begin{cases} 1 - \left|\frac{\sigma_M - \sigma_E}{\sigma_E}\right|, 0 \le \sigma_M \le \sigma_E \\ -\left(1 - \left|\frac{\sigma_M - \sigma_E}{\sigma_E}\right|\right), \sigma_E < \sigma_M \le 2\sigma_E \\ 0, \sigma_M > 2\sigma_E \end{cases}, \tag{3}$$

where σ_M and σ_E represent the weighted standard deviations derived from M and E. It is derived alongside to S_{VAR} and carries a similar physical meaning, but captures instead the standard deviation of the spatial patterns.

(4) S_{TCORR}: The temporal phase similarity metric

$$S_{TCORR} = \mathrm{r}\ , \tag{4}$$

where r represents the Pearson correlation coefficient of the two temporal variations derived from M and E. Like S_{SCORR}, values of 1 and -1 indicate perfect positive and negative linear association, respectively.

(5) S_{PSD}: The spectral similarity metric

$$S_{PSD} = \frac{\sum_{i=1}^{n} min(\mathrm{P}_{Mi}, \mathrm{P}_{Ei})}{\sum_{i=1}^{n} \mathrm{P}_{Ei}}, \tag{5}$$

where P_{Mi} and P_{Ei} are the power spectral density (PSD) values at frequency i of the PCs derived from M and E. This metric quantifies the degree to which the frequency-domain energy distribution of M matches that of E, with $S_{PSD} = 1$ indicating perfect spectral overlap and $S_{PSD} = 0$ indicating no overlap.

3 Results

3.1 Establishing a robust baseline: The emergent warming-linked CLT trend mode in reanalyses

An EOF analysis of global annual TAS and CLT anomalies from ERA5 (1979–2014) yields four distinct modes (Fig. 1). The leading TAS mode (Fig. 1a–b) captures the canonical global warming pattern: its PC correlates strongly with GMST ($r = 0.94$, $p < 0.05$, two-tailed), and its spatial pattern reproduces the well-established non-uniform warming, including the land-ocean contrast and Arctic amplification (Forster et al., 2021). In contrast, the second TAS mode (Fig. 1c–d) and the leading CLT mode (Fig. 1e–f) are dominated by internal variability; their PCs track the Niño 3.4 index closely ($r = 0.85$ for TAS-PC2, $r = 0.92$ for CLT-PC1; $p < 0.05$ for both, two-tailed), and their spatial patterns reflect well-documented ENSO teleconnections (Wang & Su, 2015; Geng et al., 2022; Liu et al., 2023). While these modes provide a fundamental test of a model's dynamical fidelity in capturing the global warming and ENSO signals in both temperature and clouds, the second CLT mode (Fig. 1g–h) is the one that isolates the large-scale cloud response to historical warming: its PC exhibits a pronounced secular increase tightly tightly coupled to GMST ($r = 0.85$, $p < 0.05$, two-tailed), and its spatial pattern displays a sharp land-ocean asymmetry, with widespread CLT increases over oceans against predominantly decreasing CLT over land.

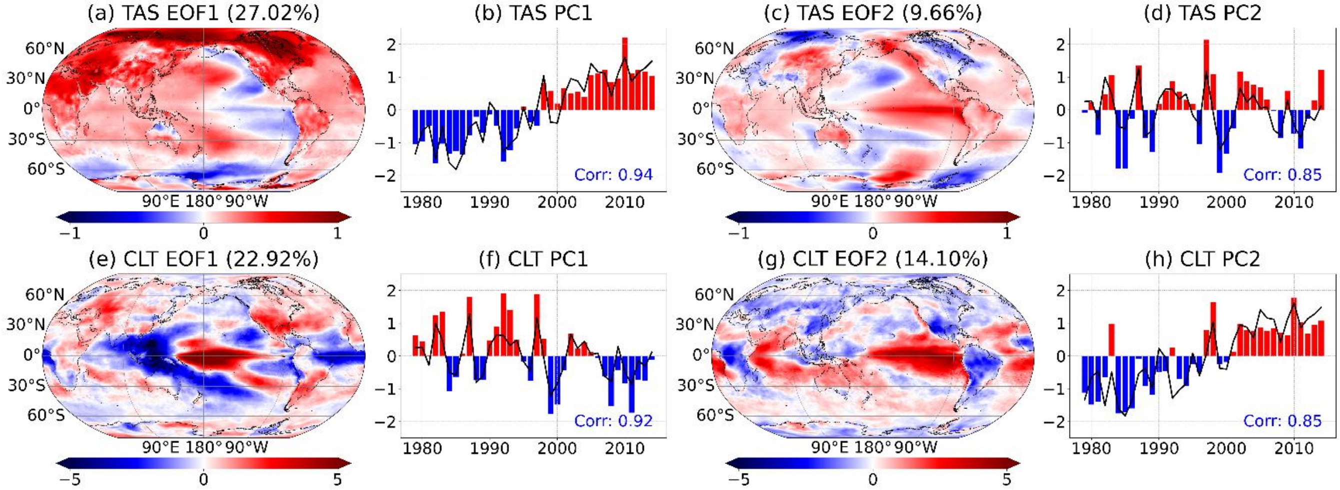

Figure 1: The two leading modes of annual TAS (units: °C) and CLT (units: %) anomalies from ERA5 for 1979–2014. (a, b) The first TAS mode (EOF1 and PC1). (c, d) The second TAS mode (EOF2 and PC2). (e, f) The first CLT mode (EOF1 and PC1). (g, h) The second CLT mode (EOF2 and PC2). All PCs are standardized, and the EOFs are scaled by the standard deviation of their corresponding PCs. The percentage in parentheses in panels (a), (c), (e), and (g) indicates the variance explained by each mode. In the PC panels (b, d, f, h), red and blue bars denote positive and negative values, respectively. In (b) and (h), the black line shows the standardized global area-weighted mean TAS series (i.e., GMST) calculated from ERA5; the number in the bottom-right corner is the correlation coefficient (r) between the PC and GMST. In (d) and (f), the black line shows the annual Niño 3.4 index; the number gives the correlation between the PC and the index.

To account for the structural uncertainties inherent in reanalysis-derived CLT, we extend the EOF analysis to three additional products (MERRA-2, CRA1.5 and R-2). Despite differences in their data assimilation and cloud parameterization schemes, a CLT mode with a pronounced secular trend in its PC consistently emerges across all datasets (Fig.2e). This cross-product consistency supports that the warming-linked trend mode identified in ERA5 is not a single-system artifact but a product-independent signal. Nevertheless, notable inter-product discrepancies remain: the explained variance ranges from ~11% to ~26%, and the spatial patterns diverge substantially (Fig. 2a–d). These inconsistencies highlight the intrinsic uncertainty in reconstructing the historical forced CLT response and necessitate the identification of its most reliable representation.

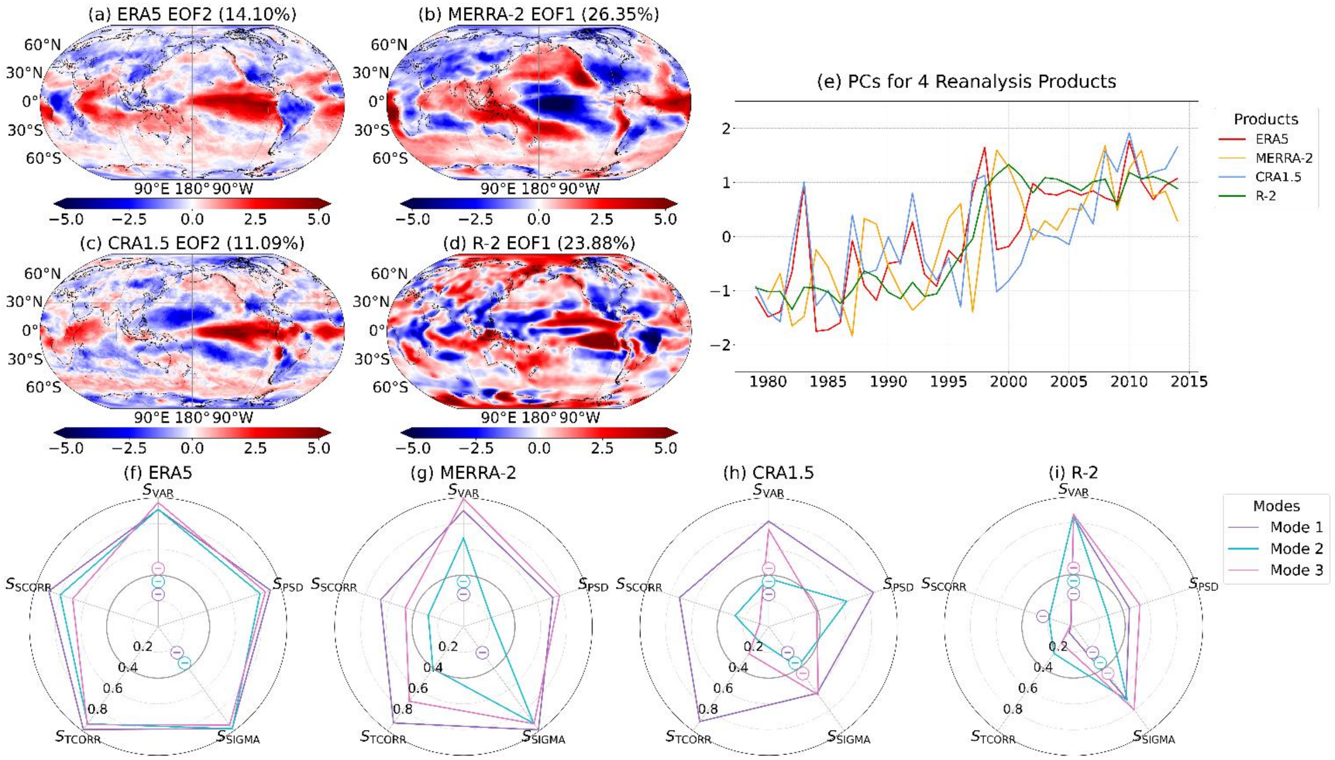

Figure 2: Robustness of the CLT trend mode across reanalyses and evaluation against MODIS observations. (a–d) EOFs of the CLT trend mode (units: %) for 1979–2014 derived from (a) ERA5, (b) MERRA-2 (1980–2014), (c) CRA1.5, and (d) R-2. (e) Corresponding standardized PCs illustrating the trending signals. (f–i) Radar diagrams comparing 5 similarity metrics between the 3 leading EOF modes of MODIS (2003–2021) and those of the reanalyses: (f) ERA5, (g) MERRA-2, (h) CRA1.5, and (i) R-2. Each colored polygon represents a specific mode [Mode 1 (purple), Mode 2 (blue), Mode 3 (pink)], with each radial axis denoting a given metric. Negative values are indicated by mode-specific colored "−" signs placed on the corresponding metric axes.

Given these discrepancies and the lack of sufficiently long, homogeneous satellite records (Stubenrauch et al., 2013; Karlsson & Devasthale, 2018) to directly validate large-scale long-term trends, we restrict such evaluation to the MODIS–reanalysis overlapping period (2003 – 2021). A reanalysis must accurately reproduce the fundamental spatiotemporal structures of observed cloud variability to serve as a credible baseline for extracting forced trends. To quantify this fidelity objectively, the three leading CLT EOF modes from each reanalysis are evaluated against MODIS using the five similarity metrics (Fig. 2f–i; Section 2.3). Among the reanalyses, ERA5 exhibits the highest fidelity, achieving similarity scores of 0.7–1.0 across all metrics (Fig. 2f), consistent with Liu et al. (2023). This robust agreement hence lends strong credibility to the longer-term trend mode derived from ERA5.

In summary, we hence establish a four-mode benchmark based exclusively on ERA5 data (1979–2014). This framework integrates the TAS warming mode, which serves as the thermodynamic baseline, alongside the ENSO-linked TAS and CLT modes that characterize internal dynamics. Complementing these is the CLT trend mode, which represents our most reliable estimate of the highly uncertain forced cloud response. Together, these four components (Fig. 1) form a comprehensive and physically meaningful framework for evaluating AMIP simulations.

3.2 The consistent absence of the warming-linked CLT mode in AMIP simulations

To maximize the signal-to-noise ratio, we first construct a multi-model mean (MMM) by averaging annual anomalies across all 13 AMIP simulations and apply EOF analysis to this aggregated field (Fig. 3). Using the four-mode benchmark established earlier, we then assess how faithfully these models reproduce the targeted climate states. This evaluation is facilitated by radar diagrams (Fig. 4), which quantitatively compare the similarity of both the MMM and individual models against the ERA5 reference across the five similarity metrics.

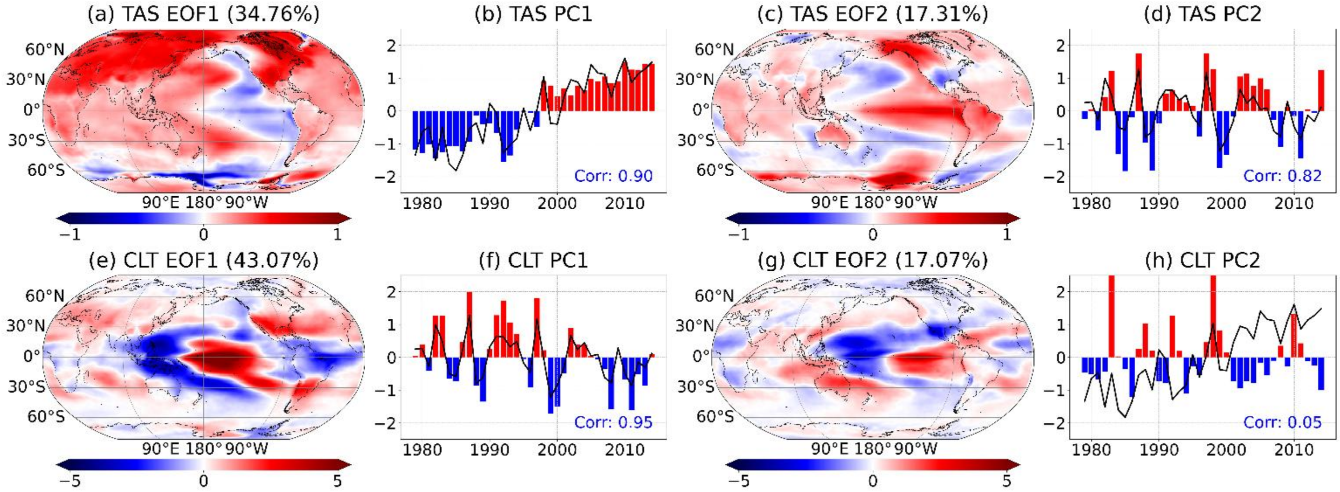

Figure 3: Same as Fig. 1 but for MMM.

The MMM exhibits high fidelity for the TAS warming mode and the ENSO-linked modes, capturing the major spatial patterns and temporal evolutions observed in ERA5 (compare Fig. 3a–f and Fig. 1a–f). While the explained variances of these MMM modes are artificially elevated by the averaging process, a caveat not applicable to individual models, their spatial and temporal similarity scores remain exceptionally high (0.8–1.0 across relevant metrics; Fig. 4a). This confirms the models' baseline capability in simulating large-scale thermodynamic changes and dominant internal variability. However, the MMM fails to reproduce the warming-linked CLT trend mode (Fig. 3g–h). Its PC lacks a systematic long-term trend, resulting in a near-zero correlation with GMST ($r = 0.05$, $p = 0.77$, two-tailed; Fig. 3h). Consequently, this mode exhibits only weak correlations of its spatial and temporal patterns with those of the ERA5 benchmark (~0.4 for S_{SCORR} and S_{TCORR}; Fig. 4a).

https://doi.org/10.5194/egusphere-2026-3175
Preprint. Discussion started: 3 July 2026

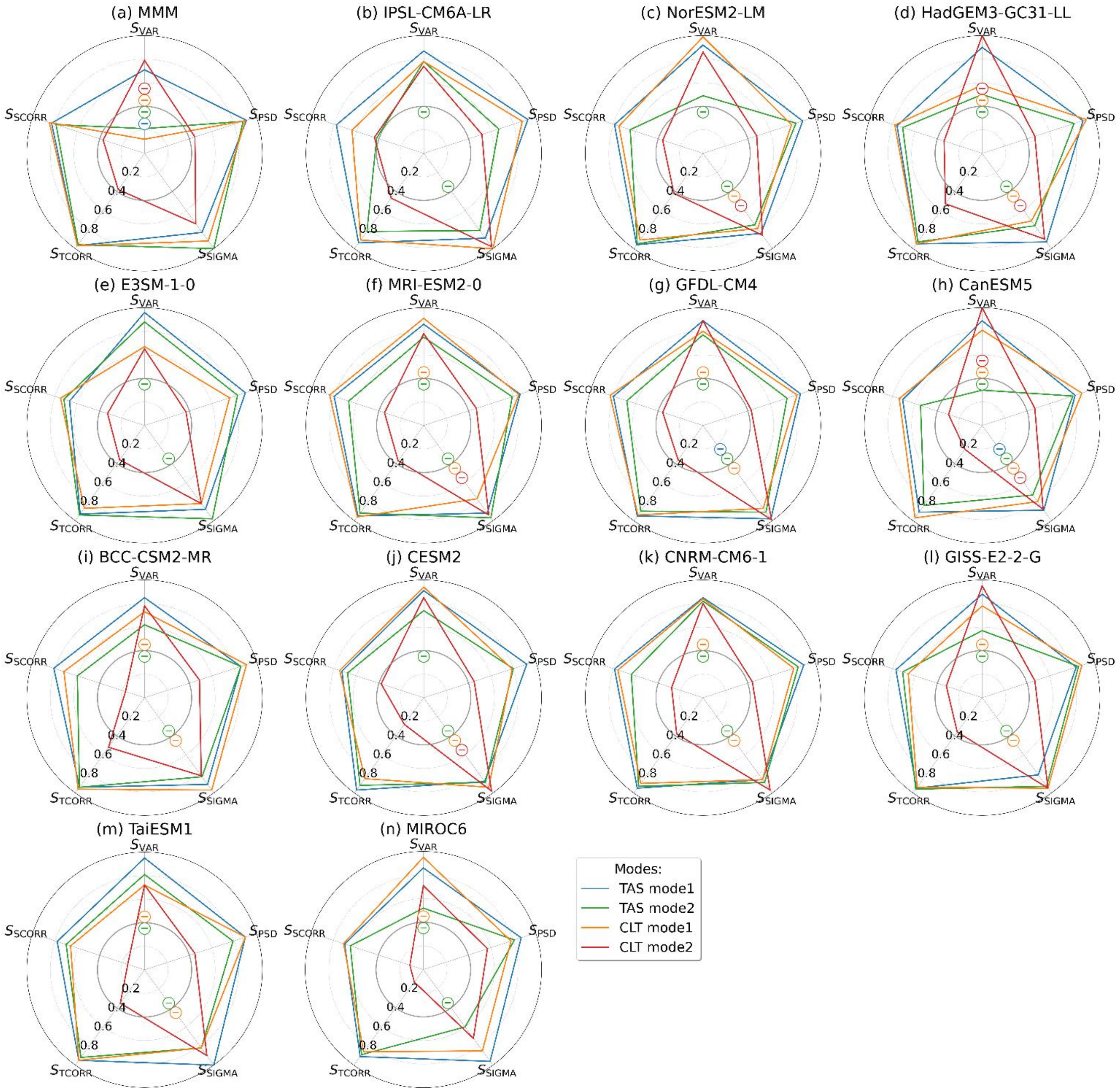

Figure 4: Radar diagrams comparing 5 similarity metrics between ERA5 modes (EOFs and PCs) and (a) the MMM, as well as (b–n) the 13 individual models. Each colored polygon represents a specific mode [TAS mode 1 (blue), TAS mode 2 (green), CLT mode 1 (orange), CLT mode 2 (red)], with each radial axis denoting a given metric. Negative values are indicated by mode-specific colored "−" signs placed on the corresponding metric axes.

Crucially, this asymmetric performance, characterized by high fidelity in the baseline modes yet coupled with the absence of the warming-linked cloud trend mode, is not an artifact of ensemble averaging. An evaluation of the 13 individual models (Fig.

4b–n) shows that every model exhibits this deficiency, with mean S_{SCORR} and S_{TCORR} values for the second CLT mode that are no higher than those of the MMM, despite their diverse dynamical cores, resolutions, and parameterizations. This rules out model-specific errors and reveals a fundamental limitation within the free-running AMIP framework: a systematic inability to convert the observed historical warming signal into the coherent cloud trends captured by multiple reanalysis products.

3.3 Spatial mismatches and amplitude deficits in the warming-linked AMIP CLT response

Given the consistent absence of the warming-linked CLT trend mode in the free-running AMIP simulations, a direct mode-to-mode comparison is precluded. To establish a common evaluation baseline, we instead adopt a linear regression approach (Wilks, 2011), regressing the AMIP-simulated CLT anomalies onto the ERA5-derived warming index (i.e., PC2 of CLT, Fig. 1h). The resulting regression patterns and corresponding three similarity metrics (excluding the two for temporal variations) are shown in Figs. 5 and 6, with those in Fig. 6 partitioned into global, oceanic, and land domains to assess the pronounced land-ocean asymmetry.

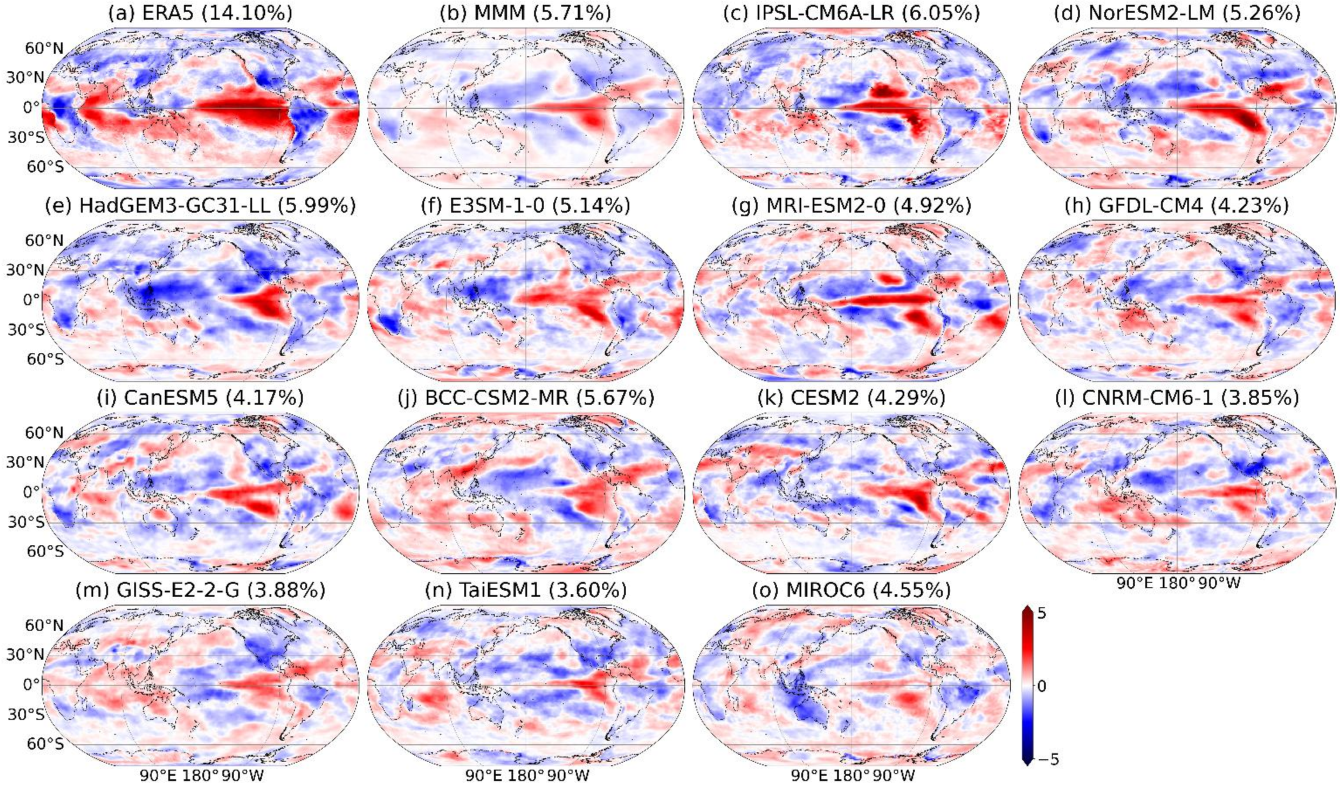

Figure 5: ERA5 CLT EOF2 and corresponding regression patterns derived from the MMM and individual models. (a) ERA5 CLT EOF2 (unit: %) for 1979–2014, as Fig. 1g. (b) Regression pattern of MMM CLT anomalies onto the ERA5 PC2 for 1979–2014. (c–o) Same as (b) but for the 13 individual models. Panels (c–o) are arranged in descending order based on the sum of the 3 global similarity metrics shown in Fig. 6a.

As illustrated in Fig. 5, the regression fails to overcome the models' inability to reproduce the CLT response to historical warming. While individual models do capture some isolated regional features, the signal's hallmark spatial signature, widespread low-latitude oceanic increases coupled with continental decreases, is spatially displaced. Most notably, the expansive positive trends across the Indian and the Atlantic Oceans are largely absent or shifted. This profound spatial mismatch yields only marginal metric improvements: compared to the free-running EOF analysis, the regression merely raises the MMM S_{SCORR} from ~0.4 to ~0.6 and the mean individual model S_{SCORR} from ~0.3 to ~0.4 (Fig. 4; Fig. 6a). Given that the free-running EOF-derived CLT mode (Fig. 3g) lacking any long-term trend already reaches this ~0.4 threshold, these gains are of limited diagnostic value. This ultimately underscores a fundamental difficulty of current climate models in reproducing the coherent spatial structure of the ERA5 benchmark.

Alongside the spatial mismatch, models exhibit a systematic underestimation of signal amplitude: even when regressed onto the warming index, individual runs yield an S_{SIGMA} of ~0.6 relative to ERA5 (Fig. 6a), indicating a 40% deficit in signal amplitude. This value further drops to ~0.4 for the MMM (Fig. 6a), reflecting severe inter-model spatial disagreement that drives the regressed CLT response toward near-zero amplitudes across most regions outside the low-latitude Pacific (Fig. 5b). This amplitude deficit directly translates into a drastic reduction in explained variance. In individual AMIP simulations, the regression trends account for only ~5% of the total CLT variance, falling far short of the ~14% captured by ERA5. This variance deficit is particularly notable given that the models successfully reproduce the ENSO-linked CLT variance (~25% versus ~23% in ERA5). Because standard EOF inherently maximizes explained variance, such an attenuated signal (~5%) not only relegates the warming-linked trend to lower-order modes but, more critically, may also preclude its emergence as an independent, spatially coherent pattern in the free-running state.

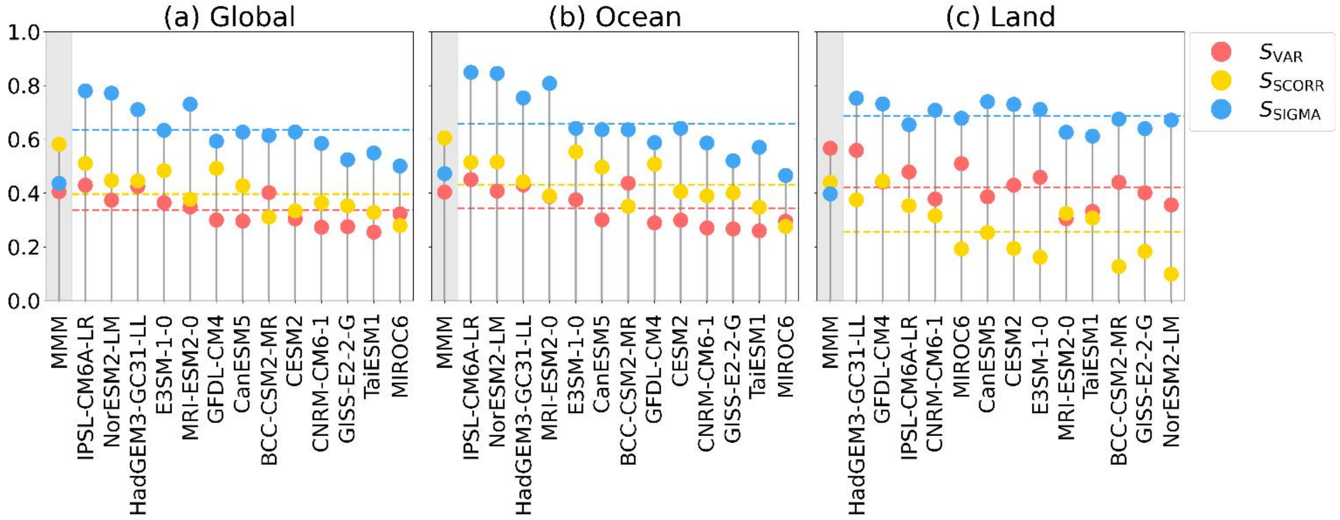

Figure 6: Scatter plots comparing 3 similarity metrics between ERA5 CLT EOF2 and the regression patterns of the MMM and 13 individual models across (a) global, (b) oceanic and (c) land domains. Oceanic and terrestrial scores are derived from masked regression patterns. Each model is represented by 3 colored dots corresponding to the metrics: [S_{VAR} (red), S_{SCORR} (yellow), and S_{SIGMA} (blue)], with dashed horizontal lines indicating the mean scores of the 13 models. In each panel, the MMM is displayed first, followed by individual models arranged in descending order of their sum of the 3 similarity metrics.

https://doi.org/10.5194/egusphere-2026-3175
Preprint. Discussion started: 3 July 2026

Beyond these systematic discrepancies, the regression-based evaluation also reveals a distinct regional asymmetry in model performance. According to the aggregated similarity metrics, IPSL-CM6A-LR ranks highest globally, while MIROC6 ranks lowest (Fig. 6a). Because oceans dominate the analyzed surface area (~70%), these global rankings closely mirror the oceanic rankings. Over the ocean, top-performing models like IPSL-CM6A-LR best capture the expansive, warming-linked CLT pattern, particularly the positive Pacific trend (Fig. 5c), yielding relatively high oceanic S_{SCORR} values of ~0.5 (Fig. 6b). Over land, however, the performance rankings undergo a substantial reordering. This reordering is systematically linked to model type: GCMs tend to outperform ESMs in simulating terrestrial CLT trends. For example, the globally top-ranked ESM, NorESM2-LM, exhibits considerably lower skill over land, whereas the relatively lower-ranked GCM, GFDL-CM4, emerges as a stronger terrestrial performer. Furthermore, spatial agreement between the AMIP and ERA5 patterns systematically deteriorates over land, mirroring the well-documented land-ocean contrast in climate models (Christopoulos and Schneider, 2021; Chen et al., 2022). Quantitatively, the land-mean S_{SCORR} drops to only ~0.26, accompanied by a greater inter-model spread (Fig. 6c), indicating a persistent difficulty in replicating the spatial distribution of warming-linked CLT trends over continental regions.

4 Conclusion and Discussion

This study establishes a four-mode benchmark that reveals a significant asymmetry in the systematic performance of 13 CMIP6 AMIP simulations: while models robustly reproduce the warming and ENSO-linked variability modes, they exhibit a systematic inability to capture the warming-linked CLT trend mode. Diagnostic regression reveals that this absence manifests as a substantial underestimation of the response amplitude and large-scale spatial mismatches. In AMIP simulations, the warming-linked CLT response anomaly accounts for only ~5% of the total variance, falling far short of the ~14% captured by ERA5. Spatially, models largely fail to reproduce the expansive marine CLT increases and widespread continental CLT decreases. These failures occur despite models' higher fidelity over oceans than over land, and despite the tendency of GCMs to outperform ESMs in simulating terrestrial cloud responses.

Although using ERA5 as a reference carries uncertainties inherent in model-informed reanalyses (Hersbach et al., 2020; Yao et al., 2020), the mode's recurrence across multiple independent datasets argues for a physically robust origin rather than an ERA5-specific artifact. Furthermore, validation against MODIS observations corroborates the reasonableness of the ERA5 representation as a reference. Consequently, within the scope of this study, the ERA5-derived mode serves as the best available estimate. The systematic failure to reproduce this mode across all AMIP simulations, including top-ranked models recognized for superior cloud simulations (e.g., IPSL-CM6A-LR and GFDL-CM4; Shin et al., 2017; Madeleine et al., 2020; Chao et al., 2024), hence points to a root cause that lies not in individual parameterization refinements but in structural limitations inherent to the free-running AMIP framework.

This structural limitation, rooted in the free-running nature of AMIP, may be illuminated by contrasting reanalyses with AMIP models. Although differences in resolution and parameterizations preclude definitive attribution, a key distinction lies in the

https://doi.org/10.5194/egusphere-2026-3175
Preprint. Discussion started: 3 July 2026

continuous observational constraint within reanalyses. This constraint likely anchors the model state to observed thermodynamic and dynamic evolutions, thereby inhibiting the accumulation of systematic errors (Wikle, 2005; Hersbach et al.,2020). In AMIP, prescribed SSTs offer only partial stabilization; the unconstrained atmosphere could allow systematic drifts that attenuate coherent forced responses. Such drifts might be further amplified by parameterization designs prioritizing mean-state fidelity and fast variability statistics over sensitivity to slow forcing (Arakawa, 2004; Hourdin et al., 2017), as well as by unresolved subgrid processes (Zhao, 2014; Parishani et al., 2018; Palmer, 2001). This lack of atmospheric anchoring may partially explain the documented underestimation of low-frequency variability in simulated sea surface temperature and sea level pressure (Wills et al., 2022), and atmospheric blocking (Anstey et al., 2013; Masato et al., 2013). It may also underlie the land-ocean asymmetry observed in model performance (Christopoulos and Schneider, 2021; Chen et al., 2022). Specifically, prescribed SSTs appear to act as a macroscopic anchor that masks marine errors while exposing terrestrial deficits (Christopoulos and Schneider, 2021; Chen et al., 2022). Without such an anchor, land simulations face compounded challenges from heterogeneous surfaces and complex feedbacks (Kleidon & Renner, 2017; Forster et al., 2021). This aligns with the degraded spatial agreement and model-type dependence noted earlier. In ESMs, interactive biogeochemical modules could introduce flux biases amplified by land-atmosphere coupling (Arora et al., 2020; Spafford & MacDougall, 2021), conversely, prescribed SSTs and homogeneous ocean surface in AMIP preclude such feedbacks, potentially limiting error propagation pathways.

Given this persistent underperformance even under prescribed SSTs, our findings raise critical concerns about interpreting fully coupled CMIP6 simulations. In coupled models, apparent agreement with observed trends may reflect compensating errors between SSTs and clouds rather than true physical fidelity, potentially complicating assessments of cloud feedbacks and equilibrium climate sensitivity (Stephens, 2005; Zelinka et al., 2017; Forster et al., 2021). Resolving this structural deficiency requires at least two further steps: (1) identifying the specific cloud regimes and meteorological drivers responsible for the ~9% variance gap; and (2) to extend this diagnostic framework to fully-coupled simulations to disentangle how interactive ocean-atmosphere dynamics and inherent SST biases modulate the cloud response signal that is already attenuated in the absence of atmospheric anchoring.

Code and data availability. All analyses used to generate results are conducted by the programming languages of Python (Version 3.12.3, last access: 1 June 2026). The SciPy library (Version 1.13.1) for Pearson correlation analysis and linear regression. The eofs library (Version 1.4.1) for EOF analysis. All data used in this work is publicly available. Climate model simulations were obtained from the Earth System Grid Federation (https://aims2.llnl.gov/search, last access: 6 December 2024). ERA5 data was downloaded from the Copernicus Climate Change Service Climate Data Store (https://doi.org/10.24381/cds.f17050d7, last access: 20 October 2024). MERRA-2 data was obtained from the Goddard Earth

Sciences Data and Information Services Center (https://disc.gsfc.nasa.gov/datasets/M2TMNXRAD_5.12.4/summary, last access: 23 February 2026). CRA1.5 data was obtained from the China Meteorological Administration (CMA) National Meteorological Science Data Center (https://data.cma.cn/ai/#/detail?id=21, last access: 26 March 2026). R-2 data was obtained from the NOAA Physical Sciences Laboratory (https://psl.noaa.gov/data/gridded/data.ncep.reanalysis2.html, last access: 23 February 2026). MODIS data was obtained from NASA's Earthdata Search (https://search.earthdata.nasa.gov/search?q=MYD08_D3, last access: 19 December 2025). ENSO index (Niño 3.4) was downloaded from NOAA center (https://origin.cpc.ncep.noaa.gov/products/analysis_monitoring/ensostuff/ONI_change.shtml, last access: 8 April 2025).

Author contributions. S.M.: Formal analysis, Investigation, Writing—Original Draft. H.L.: Conceptualization, Methodology, Supervision, Funding Acquisition, Writing—Review & Editing. J.Z., X.W.: Methodology, Writing—Review & Editing. F.W., L.L.: Conceptualization, Writing—Review & Editing. All authors discussed the results, contributed to the final manuscript, and approved the submitted version.

Competing interests. The authors declare they have no conflict of interest.

Financial support. This work has been supported by the National Natural Science Foundation of China (No. 42405088), and the Innovation Research Foundation of National University of Defense Technology (No. 202401-YJRC-XX-033).

References

Aerenson, T., Marchand, R., Chepfer, H., & Medeiros, B. (2022). When will MISR detect rising high clouds? Journal of Geophysical Research: Atmospheres, 127(2), e2021JD035865. https://doi.org/10.1029/2021JD035865

Anstey, J. A., Davini, P., Gray, L. J., Woollings, T. J., Butchart, N., Cagnazzo, C., Christiansen, B., Hardiman, S. C., Osprey, S. M., & Yang, S. (2013). Multi-model analysis of Northern Hemisphere winter blocking: Model biases and the role of resolution. Journal of Geophysical Research: Atmospheres, 118(10), 3956–3971. https://doi.org/10.1002/jgrd.50231

Arora, V. K., Katavouta, A., Williams, R. G., Jones, C. D., Brovkin, V., Friedlingstein, P., Schwinger, J., Bopp, L., Boucher, O., & Cadule, P. (2020). Carbon–concentration and carbon–climate feedbacks in CMIP6 models and their comparison to CMIP5 models. Biogeosciences, 17(16), 4173–4222. https://doi.org/10.5194/bg-17-4173-2020, 2020.

Bader, D. C., Leung, R., Taylor, M., & McCoy, R. B. (2019). E3SM-Project E3SM1.0 model output prepared for CMIP6 CMIP amip [Data set]. Earth System Grid Federation. https://doi.org/10.22033/ESGF/CMIP6.4492

Arakawa, A. (2004). The cumulus parameterization problem: Past, present, and future. Journal of Climate, 17(13), 2493–2525. https://doi.org/10.1175/1520-0442(2004)017%3C2493:RATCPP%3E2.0.CO;2

Barker, H. W. (2008). Representing cloud overlap with an effective decorrelation length: An assessment using CloudSat and CALIPSO data. Journal of Geophysical Research: Atmospheres, 113(D24), 2008JD010391. https://doi.org/10.1029/2008JD010391

Boucher, O., Denvil, S., Levavasseur, G., Cozic, A., Caubel, A., Foujols, M.-A., Meurdesoif, Y., Cadule, P., Devilliers, M., Ghattas, J., Lebas, N., Lurton, T., Mellul, L., Musat, I., Mignot, J., & Cheruy, F. (2018). IPSL IPSL-CM6A-LR model output prepared for CMIP6 CMIP amip [Data set]. Earth System Grid Federation. https://doi.org/10.22033/ESGF/CMIP6.5113

Ceppi, P., Myers, T. A., Nowack, P., Wall, C. J., & Zelinka, M. D. (2024). Implications of a Pervasive Climate Model Bias for Low-Cloud Feedback. Geophysical Research Letters, 51(20), e2024GL110525. https://doi.org/10.1029/2024GL110525

Cess, R., Potter, G., Blanchet, J.-P., Boer, G., Delgenio, A., DÃ©quÃ©, M., Dymnikov, V., Galin, V., Gates, W., Ghan, S., Kiehl, J., Lacis, A., Treut, H., Li, Z.-X., Liang, X.-Z., McAvaney, B., Meleshko, V., Mitchell, J., Morcrette, J.-J., & Zhang, M.-H. (1990). Intercomparison and interpretation of climate feedback processes in 19 atmospheric general circulation models. J. Geophys. Res., 95, 16601–16615. https://doi.org/10.1029/JD095iD10p16601

Chao, L., Zelinka, M. D., & Dessler, A. E. (2024). Evaluating Cloud Feedback Components in Observations and Their Representation in Climate Models. Journal of Geophysical Research: Atmospheres, 129(2), e2023JD039427. https://doi.org/10.1029/2023JD039427

Chen, G., Wang, W., Bao, Q., & Li, J. (2022). Evaluation of Simulated Cloud Diurnal Variation in CMIP6 Climate Models. Journal of Geophysical Research: Atmospheres, 127(6), e2021JD036422. https://doi.org/10.1029/2021JD036422

Chepfer, H., Noel, V., Winker, D., & Chiriaco, M. (2014). Where and when will we observe cloud changes due to climate warming? Geophysical Research Letters, 41(23), 8387–8395. https://doi.org/10.1002/2014GL061792

Christopoulos, C., & Schneider, T. (2021). Assessing Biases and Climate Implications of the Diurnal Precipitation Cycle in Climate Models. Geophysical Research Letters, 48(13), e2021GL093017. https://doi.org/10.1029/2021GL093017

Coburn, J., & Pryor, S. C. (2021). Differential Credibility of Climate Modes in CMIP6. Journal of Climate, 34(20), 8145–8164. https://doi.org/10.1175/JCLI-D-21-0359.1

Danabasoglu, G. (2019). NCAR CESM2 model output prepared for CMIP6 CMIP amip [Data set]. Earth System Grid Federation. https://doi.org/10.22033/ESGF/CMIP6.7522

Enriquez-Alonso, A., Sanchez-Lorenzo, A., Calbó, J., González, J.-A., & Norris, J. R. (2016). Cloud cover climatologies in the Mediterranean obtained from satellites, surface observations, reanalyses, and CMIP5 simulations: Validation and future scenarios. Climate Dynamics, 47(1–2), 249–269. https://doi.org/10.1007/s00382-015-2834-4

Eyring, V., Bony, S., Meehl, G. A., Senior, C. A., Stevens, B., Stouffer, R. J., & Taylor, K. E. (2016). Overview of the Coupled Model Intercomparison Project Phase 6 (CMIP6) experimental design and organization. Geoscientific Model Development, 9(5), 1937–1958. https://doi.org/10.5194/gmd-9-1937-2016

Forster, P., Storelvmo, T., Armour, K., Collins, W., Dufresne, J.-L., Frame, D., Lunt, D. J., Mauritsen, T., Palmer, M. D., Watanabe, M., Wild, M., & Zhang, H. (2021). The Earth's energy budget, climate feedbacks, and climate sensitivity. In V. Masson-Delmotte et al. (Eds.), Climate change 2021: The physical science basis. Contribution of Working Group I to the Sixth Assessment Report of the Intergovernmental Panel on Climate Change (pp. 923–1054). Cambridge, United Kingdom and New York, NY: Cambridge University Press. https://doi.org/10.1017/9781009157896.009

Guo, H., John, J. G., Blanton, C., McHugh, C., Nikonov, S., Radhakrishnan, A., Rand, K., Zadeh, N. T., Balaji, V., Durachta, J., Dupuis, C., Menzel, R., Robinson, T., Underwood, S., Vahlenkamp, H., Bushuk, M., Dunne, K. A., Dussin, R., Gauthier, P. P., … Zhang, R. (2018). NOAA-GFDL GFDL-CM4 model output amip [Data set]. Earth System Grid Federation.

Geng, T., Cai, W., Wu, L., Santoso, A., Wang, G., Jing, Z., Gan, B., Yang, Y., Li, S., Wang, S., Chen, Z., & McPhaden, M. J. (2022). Emergence of changing Central-Pacific and Eastern-Pacific El Niño-Southern Oscillation in a warming climate. Nature Communications, 13(1), 6616. https://doi.org/10.1038/s41467-022-33930-5

Global Modeling and Assimilation Office (GMAO). (2015). MERRA-2 tavgM_2d_rad_Nx: 2d, Monthly mean, Time-Averaged, Single-Level, Assimilation, Radiation Diagnostics V5.12.4 [Dataset]. Goddard Earth Sciences Data and Information Services Center (GES DISC). https://doi.org/10.5067/OU3HJDS973O0

Gulev, S. K., Thorne, P. W., Ahn, J., Dentener, F. J., Domingues, C. M., Gerland, S., Gong, D., Kaufman, D. S., Nnamchi, H. C., Quaas, J., Rivera, J. A., Sathyendranath, S., Smith, S. L., Trewin, B., von Schuckmann, K., & Vose, R. S. (2021). Changing state of the climate system. In V. Masson-Delmotte et al. (Eds.), Climate change 2021: The physical science basis. Contribution of Working Group I to the Sixth Assessment Report of the Intergovernmental Panel on Climate Change (pp. 287–422). Cambridge, United Kingdom and New York, NY: Cambridge University Press. https://doi.org/10.1017/9781009157896.004

Hannachi, A., Jolliffe, I. T., & Stephenson, D. B. (2007). Empirical orthogonal functions and related techniques in atmospheric science: A review. International Journal of Climatology, 27(9), 1119–1152. https://doi.org/10.1002/joc.1499

Hersbach, H., Bell, B., Berrisford, P., Biavati, G., Horányi, A., Muñoz Sabater, J., Nicolas, J., Peubey, C., Radu, R., Rozum, I., Schepers, D., Simmons, A., Soci, C., Dee, D., & Thépaut, J.-N. (2023). ERA5 monthly averaged data on single levels from 1940 to present [Dataset]. Copernicus Climate Change Service (C3S) Climate Data Store (CDS). https://doi.org/10.24381/cds.f17050d7

Hersbach, H., Bell, B., Berrisford, P., Hirahara, S., & Jean ㎞ ol Thépaut. (2020). The ERA5 global reanalysis. Quarterly Journal of the Royal Meteorological Society. https://doi.org/10.1002/qj.3803

Hourdin, F., Mauritsen, T., Gettelman, A., Golaz, J.-C., Balaji, V., Duan, Q., Folini, D., Ji, D., Klocke, D., & Qian, Y. (2017). The art and science of climate model tuning. Bulletin of the American Meteorological Society, 98(3), 589–602. https://doi.org/10.1175/BAMS-D-15-00135.1

Kanamitsu, M., Ebisuzaki, W., Woollen, J., Yang, S.-K., Hnilo, J. J., Fiorino, M., & Potter, G. L. (2002). NCEP-DOE AMIP-II Reanalysis (R-2). Bulletin of the American Meteorological Society, 83(11), 1631–1643. https://doi.org/10.1175/BAMS-83-11-1631

Karlsson, K.-G., & Devasthale, A. (2018). Inter-comparison and evaluation of the four longest satellite-derived cloud climate data records: CLARA-A2, ESA Cloud CCI V3, ISCCP-HGM, and PATMOS-x. Remote Sensing, 10(10), 1567. https://doi.org/10.3390/rs10101567

Kleidon, A., & Renner, M. (2017). An explanation for the different climate sensitivities of land and ocean surfaces based on the diurnal cycle. Earth System Dynamics, 8(3), 849–864. https://doi.org/10.5194/esd-8-849-2017

Lee, W.-L., & Liang, H.-C. (2019). AS-RCEC TaiESM1.0 model output prepared for CMIP6 CMIP amip [Data set]. Earth System Grid Federation. https://doi.org/10.22033/ESGF/CMIP6.9713

Liu, H., Koren, I., Altaratz, O., & Chekroun, M. D. (2023). Opposing trends of cloud coverage over land and ocean under global warming. Atmospheric Chemistry and Physics, 23(11), 6559–6569. https://doi.org/10.5194/acp-23-6559-2023

Madeleine, J., Hourdin, F., Grandpeix, J., Rio, C., Dufresne, J., Vignon, E., Boucher, O., Konsta, D., Cheruy, F., Musat, I., Idelkadi, A., Fairhead, L., Millour, E., Lefebvre, M., Mellul, L., Rochetin, N., Lemonnier, F., Touzé-Peiffer, L., & Bonazzola, M. (2020). Improved Representation of Clouds in the Atmospheric Component LMDZ6A of the IPSL-CM6A Earth System Model. Journal of Advances in Modeling Earth Systems, 12(10), e2020MS002046. https://doi.org/10.1029/2020MS002046

Masato, G., Hoskins, B. J., & Woollings, T. (2013). Winter and summer Northern Hemisphere blocking in CMIP5 models. Journal of Climate, 26(18), 7044–7059. doi:10.1175/JCLI-D-12-00466.1

NASA Goddard Institute for Space Studies (NASA/GISS) (2019). NASA-GISS GISS-E2-2-G model output prepared for CMIP6 CMIP amip [Data set]. Earth System Grid Federation. https://doi.org/10.22033/ESGF/CMIP6.6986

Norris, J. R., & Evan, A. T. (2015). Empirical removal of artifacts from the ISCCP and PATMOS-x satellite cloud records. Journal of Atmospheric and Oceanic Technology, 32(4), 691–702. https://doi.org/10.1175/JTECH-D-14-00058.1

Norris, J. R., Allen, R. J., Evan, A. T., Zelinka, M. D., O'Dell, C. W., & Klein, S. A. (2016). Evidence for climate change in the satellite cloud record. Nature, 536(7614), 72–75. https://doi.org/10.1038/nature18273

Palmer, T. N. (2001). A nonlinear dynamical perspective on model error: A proposal for non-local stochastic-dynamic parametrization in weather and climate prediction models. Quarterly Journal of the Royal Meteorological Society, 127(572), 279–304. https://doi.org/10.1002/qj.49712757202

Parishani, H., Pritchard, M. S., Bretherton, C. S., Terai, C. R., Wyant, M. C., Khairoutdinov, M., & Singh, B. (2018). Insensitivity of the Cloud Response to Surface Warming Under Radical Changes to Boundary Layer Turbulence and Cloud Microphysics: Results From the Ultraparameterized CAM. Journal of Advances in Modeling Earth Systems, 10(12), 3139–3158. https://doi.org/10.1029/2018MS001409

Platnick, S. (2015). MODIS Atmosphere L3 Daily Product [Dataset]. NASA MODIS Adaptive Processing System, Goddard Space Flight Center, USA, NASA Earch Data. https://doi.org/10.5067/MODIS/MYD08_D3.061.

Probst, P., Rizzi, R., Tosi, E., Lucarini, V., & Maestri, T. (2012). Total cloud cover from satellite observations and climate models. Atmospheric Research, 107, 161–170. https://doi.org/10.1016/j.atmosres.2012.01.005

Qian, Y., Long, C. N., Wang, H., Comstock, J. M., McFarlane, S. A., & Xie, S. (2012). Evaluation of cloud fraction and its radiative effect simulated by IPCC AR4 global models against ARM surface observations. Atmospheric Chemistry and Physics, 12(4), 1785–1810. https://doi.org/10.5194/acp-12-1785-2012

Ridley, J., Menary, M., Kuhlbrodt, T., Andrews, M., & Andrews, T. (2019). MOHC HadGEM3-GC31-LL model output prepared for CMIP6 CMIP amip [Data set]. Earth System Grid Federation. https://doi.org/10.22033/ESGF/CMIP6.5853

Ringer, M. A., Andrews, T., & Webb, M. J. (2014). Global-mean radiative feedbacks and forcing in atmosphere-only and coupled atmosphere-ocean climate change experiments. Geophysical Research Letters, 41(11), 4035–4042. http://dx.doi.org/10.1002/2014GL060347

Schiemann, R., Demory, M.-E., Shaffrey, L. C., Strachan, J., Vidale, P. L., Mizielinski, M. S., Roberts, M. J., Matsueda, M., Wehner, M. F., & Jung, T. (2017). The resolution sensitivity of Northern Hemisphere blocking in four 25-km atmospheric global circulation models. Journal of Climate, 30(1), 337–358. https://doi.org/10.1175/JCLI-D-16-0100.1

Seland, Ø., Bentsen, M., Olivié, D. J. L., Toniazzo, T., Gjermundsen, A., Graff, L. S., Debernard, J. B., Gupta, A. K., He, Y., Kirkevåg, A., Schwinger, J., Tjiputra, J., Aas, K. S., Bethke, I., Fan, Y., Griesfeller, J., Grini, A., Guo, C., Ilicak, M., … Schulz, M. (2019). NCC NorESM2-LM model output prepared for CMIP6 CMIP amip [Data set]. Earth System Grid Federation.

Shin, S.-H., Kim, O.-Y., Kim, D., & Lee, M.-I. (2017). Cloud radiative effects and changes simulated by the Coupled Model Intercomparison Project Phase 5 models. Advances in Atmospheric Sciences, 34(7), 859–876. https://doi.org/10.1007/s00376-017-6089-3

Spafford, L., & MacDougall, A. H. (2021). Validation of terrestrial biogeochemistry in CMIP6 Earth system models: A review. Geoscientific Model Development Discussions, 2021, 1–51. https://doi.org/10.5194/gmd-14-5863-2021

Stephens, G. L. (2005). Cloud feedbacks in the climate system: A critical review. Journal of Climate, 18(2), 237–273. https://doi.org/10.1175/JCLI-3243.1

Stubenrauch, C. J., Rossow, W. B., Kinne, S., Ackerman, S., Cesana, G., Chepfer, H., Di Girolamo, L., Getzewich, B., Guignard, A., & Heidinger, A. (2013). Assessment of global cloud datasets from satellites: Project and database initiated by the GEWEX radiation panel. Bulletin of the American Meteorological Society, 94(7), 1031–1049. https://doi.org/10.1175/BAMS-D-12-00117.1

Swart, N. C., Cole, J. N. S., Kharin, V. V., Lazare, M., Scinocca, J. F., Gillett, N. P., Anstey, J., Arora, V., Christian, J. R., Jiao, Y., Lee, W. G., Majaess, F., Saenko, O. A., Seiler, C., Seinen, C., Shao, A., Solheim, L., von Salzen, K., Yang, D., … Sigmond, M. (2019). CCCma CanESM5 model output prepared for CMIP6 CMIP amip [Data set]. Earth System Grid Federation. https://doi.org/10.22033/ESGF/CMIP6.3535

Voldoire, A. (2018). CNRM-CERFACS CNRM-CM6-1 model output prepared for CMIP6 CMIP amip [Data set]. Earth System Grid Federation. https://doi.org/10.22033/ESGF/CMIP6.3922

Tatebe, H., & Watanabe, M. (2018). MIROC MIROC6 model output prepared for CMIP6 CMIP amip [Data set]. Earth System Grid Federation. https://doi.org/10.22033/ESGF/CMIP6.5422

Wang, H., & Su, W. (2013). Evaluating and understanding top of the atmosphere cloud radiative effects in Intergovernmental Panel on Climate Change (IPCC) Fifth Assessment Report (AR5) Coupled Model Intercomparison Project Phase 5 (CMIP5) models using satellite observations. Journal of Geophysical Research: Atmospheres, 118(2), 683–699. https://doi.org/10.1029/2012JD018619

Wang, H., & Su, W. (2015). The ENSO effects on tropical clouds and top-of-atmosphere cloud radiative effects in CMIP5 models. Journal of Geophysical Research: Atmospheres, 120(10), 4443–4465. https://doi.org/10.1002/2014JD022337

Wang, X., Miao, H., Feng, J., & Liu, Y. (2024). Comparison of Short-Term Cloud Feedbacks at Top of the Atmosphere and the Surface in Observations and AMIP6 Models. Journal of Geophysical Research: Atmospheres, 129(2), e2023JD039936. https://doi.org/10.1029/2023JD039936

Webb, M. J., Andrews, T., Bodas-Salcedo, A., Bony, S., Bretherton, C. S., Chadwick, R., Chepfer, H., Douville, H., Good, P., Kay, J. E., Klein, S. A., Marchand, R., Medeiros, B., Siebesma, A. P., Skinner, C. B., Stevens, B., Tselioudis, G., Tsushima, Y., & Watanabe, M. (2017). The Cloud Feedback Model Intercomparison Project (CFMIP) contribution to CMIP6. Geoscientific Model Development, 10(1), 359–384. https://doi.org/10.5194/gmd-10-359-2017

Wikle, C. K. (2005). Atmospheric modeling, data assimilation, and predictability. Taylor & Francis. https://doi.org/10.1198/tech.2005.s326

Wilks, D. S. (2011). Statistical methods in the atmospheric sciences (Vol. 100). Academic press.

Wills, R. C., Dong, Y., Proistosecu, C., Armour, K. C., & Battisti, D. S. (2022). Systematic climate model biases in the large-scale patterns of recent sea-surface temperature and sea-level pressure change. Geophysical Research Letters, 49(17), e2022GL100011. https://doi.org/10.1029/2022GL100011

Wu, T., Chu, M., Dong, M., Fang, Y., Jie, W., Li, J., Li, W., Liu, Q., Shi, X., Xin, X., Yan, J., Zhang, F., Zhang, J., Zhang, L., & Zhang, Y. (2019). BCC BCC-CSM2MR model output prepared for CMIP6 CMIP amip [Data set]. Earth System Grid Federation.

Yao, B., Teng, S., Lai, R., Xu, X., Yin, Y., Shi, C., & Liu, C. (2020). Can atmospheric reanalyses (CRA and ERA5) represent cloud spatiotemporal characteristics? Atmospheric Research, 244, 105091. https://doi.org/10.1016/j.atmosres.2020.105091

Yukimoto, S., Koshiro, T., Kawai, H., Oshima, N., Yoshida, K., Urakawa, S., Tsujino, H., Deushi, M., Tanaka, T., Hosaka, M., Yoshimura, H., Shindo, E., Mizuta, R., Ishii, M., Obata, A., & Adachi, Y. (2019). MRI MRI-ESM2.0 model output prepared for CMIP6 CMIP amip [Data set]. Earth System Grid Federation. https://doi.org/10.22033/ESGF/CMIP6.6758

Zelinka, M. D., Randall, D. A., Webb, M. J., & Klein, S. A. (2017). Clearing clouds of uncertainty. Nature Climate Change, 7(10), 674–678. https://doi.org/10.1038/nclimate3402

Zhang, H., Wang, F., Wang, F., Li, J., Chen, X., Wang, Z., Li, J., Zhou, X., Wang, Q., Wang, H., You, T., Xie, B., Chen, Q., & Duan, Y. (2022). Advances in cloud radiative feedbacks in global climate change (in Chinese). Scientia Sinica Terrae, 52(3), 400–417. https://doi.org/10.1360/SSTe-2021-0052

Zhang, T., Zhou, Z., Liu, Z., Shi, C., Yao, S., Jiang, L., Yao, Y., Zhang, Z., Liang, X., & Zhang, Z. (2025). The CMA Global Atmospheric Reanalysis Version 1.5 (CRA1. 5). Journal of Meteorological Research, 39(6), 1379–1398. https://doi.org/10.1007/s13351-025-5112-3

Zhao, L., Wang, Y., Zhao, C., Dong, X., & Yung, Y. L. (2022). Compensating Errors in Cloud Radiative and Physical Properties over the Southern Ocean in the CMIP6 Climate Models. Advances in Atmospheric Sciences, 39(12), 2156–2171. https://doi.org/10.1007/s00376-022-2036-z

Zhao, M. (2014). An investigation of the connections among convection, clouds, and climate sensitivity in a global climate model. Journal of Climate, 27(5), 1845–1862. https://doi.org/10.1175/JCLI-D-13-00145.1

Zhou, T. J., Zou, L. W., & Chen, X. L. (2019). Commentary on the Coupled Model Intercomparison Project Phase 6 (CMIP6) (in Chinese). Climate Change Research, 15(5), 445–456. https://doi.org/10.12006/j.issn.1673-1719.2019.193